Anomalous Diffusion of Deformable Particles in a Honeycomb Network

Zaiyi Shen[1,2] Franck Plouraboué,[3] Juho S. Lintuvuori,[2] Hengdi Zhang,[4] Mehdi Abbasi,[1] and Chaouqi Misbah[1,*]

[1]*Université Grenoble Alpes, CNRS, LIPHY, F-38000 Grenoble, France*
[2]*Université de Bordeaux, CNRS, LOMA (UMR 5798), F-33405 Talence, France*
[3]*Institut de Mécanique des Fluides de Toulouse, IMFT, Université de Toulouse, CNRS, Toulouse, France*
[4]*Shenzhen Sibionics Co. Ltd., Shenzhen 518000, People's Republic of China*

Transport of deformable particles in a honeycomb network is studied numerically. It is shown that the particle deformability has a strong impact on their distribution in the network. For sufficiently soft particles, we observe a short memory behavior from one bifurcation to the next, and the overall behavior consists in a random partition of particles, exhibiting a diffusionlike transport. On the contrary, stiff enough particles undergo a biased distribution whereby they follow a deterministic partition at bifurcations, due to long memory. This leads to a lateral ballistic drift in the network at small concentration and anomalous superdiffusion at larger concentration, even though the network is ordered. A further increase of concentration enhances particle-particle interactions which shorten the memory effect, turning the particle anomalous diffusion into a classical diffusion. We expect the drifting and diffusive regime transition to be generic for deformable particles.

Introduction.—Transport and nutrient delivery convected by fluid flow in networks is ubiquitous in living systems, such as fungal mycelia, plant, human tissues, etc. [1,2]. The transport properties are certainly affected by the topological nature of the channel networks [3–6]. Besides network topology, the impact of other factors, like the mechanical properties of particles, is not fully understood.

At microscopic scale, the particles typically are comparable in size to the channel sizes, and the particle properties such as stiffness or shape can have profound effects on the flow behavior. The nontrivial discrete nature of the suspended elements is omnipresent in microfluidics, raising challenging issues in terms of an effective description of particle transport even in simple geometries [7–11]. Typical examples are the occurrence of disruption of the particle train via long range hydrodynamic interactions [10], as well as the emergence of large scale oscillations of droplets in a simple loop [11]. A more specific topic of interest exhibited in various microfluidic configurations is lateral-cell migration: depending on their size and deformability soft deformable cells display distinct hydrodynamical interactions with obstacles or boundaries producing cocurrent sorting [12,13]. Such mechanical based sorting is of interest since most circulating cells lie in a narrow range of sizes and shapes [13]. Furthermore, being of hydrodynamic origin lateral-cell migration permits fast, low-cost, high-throughput sorting [14]. Another example is provided by red blood cells (RBCs). At the microcirculation scale, RBCs have comparable size to vessel sizes, so that the discrete nature of the blood comes to the fore [15–21] sometimes leading to margination of stiffer RBCs [22].

Motivated by a basic understanding of the particle sorting in microscale networks, we study, numerically, the flow of deformable particles using a 2D vesicle model (also see simulations of 3D particles in [23]), in a periodic ordered network (in the form of a honeycomb), and analyze their transport properties depending on their mechanical parameters (affecting particle shape). In addition to deformable particle flows in microfluidic networks, the results can give insight on the flow of RBCs in cardiovascular systems. The predictions might be relevant in several diseases, such as sickle cell anemia or malaria. Real microvascular networks consist of many short vessel segments having lengths and widths in the range of hundreds of micrometers and a few micrometers, respectively [24,25]. These vessel lengths are not long enough to allow RBCs to achieve a permanent regime regarding their spatial organization, especially in the dilute case. In other words, the spatial pattern of RBCs in a given vessel depends on upstream history. This memory effect marks a break with the classic image [26–28] according to which the spatial organization of the suspension reaches steady state in each of the branches. As a consequence, nontrivial results, such as the manifestation of trajectories obeying anomalous diffusion laws, are revealed. A remarkable property is the fact that anomalous diffusion is not a consequence of a disorder (unlike transport, for example, in porous media [29]), but is the result of an intricate combination of particle deformation and their mutual interactions.

A systematic study, based on numerical simulations, reveals that the configurations (such as lateral position and shape) of a deformable particle in the downstream position
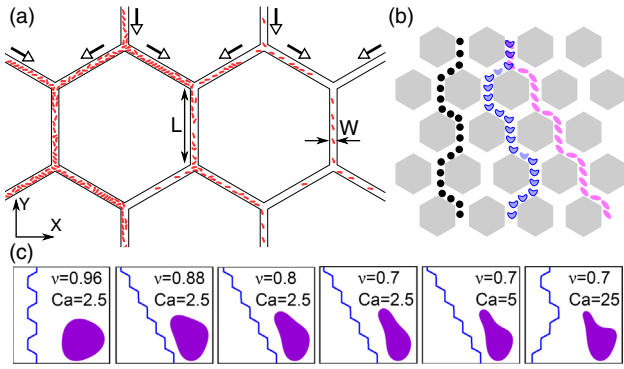
FIG. 1. (a) A snapshot showing the simulation system. The particles flow in a hexagonal network, where each segment of the channel has length L and width W. The hollow arrows show the flow directions in the channels. (b) Schematic trajectories of a rigid sphere (black), a rigid nonspherical particle (magenta), and a soft particle (blue) in the network. (c) Trajectories of a single particle in the network for different reduced area and capillary numbers. The particle shapes in the center of the feeding channel are plotted for the corresponding parameters.

depends on the previous states of the particle in the upstream position. This results in various particle configurations from one bifurcation to the next. Our study considers particles both in 2D and 3D [23]. We closely inspect individual particle dynamics and reveal that their specific trajectories impact the overall lateral transport of suspension in the network. It will be shown that, the particle lateral transport, depending on particle stiffness and concentration, covers a rich panel of behaviors from classical to anomalous diffusion and to ballistic motion. In particular, rigid particles follow a ballistic motion at small concentrations. Increasing the concentration further enhances particle-particle interactions, resulting in a crossover from anomalous to diffusionlike transport.

Model.—The suspension is injected at upper feeding vessels [vertical arrows at top surface of Fig. 1(a)] and spreads out laterally to feed the network. We consider an ordered network with hexagonal loops [Fig. 1(a)]. This is inspired by microvascular patterns, such as those encountered in mucosal capillary networks [30]. On the other hand, a regular geometry allows us to reduce the complexity and concentrate on the impact of particle mechanical properties only. A constant body force (in the $-Y$ direction) is applied to drive the fluid, with periodic boundary conditions in X and Y directions. The fluid flow is obtained from solving Navier-Stokes equations using the lattice Boltzmann method (LBM) [31]. The RBC-like particle is modeled as a vesicle with a biconcave shape using a two-dimensional spring model [31]. The reduced area is defined as $\nu = (A/\pi)/[P/(2\pi)]^2$, where A and P are the area and perimeter of the particle, respectively, and the particle radius R is defined as $\sqrt{A/\pi}$. The fluid-structure interaction is achieved by adopting the immersed boundary method [31–33].

Particle deformation is characterized by the capillary number, defined as $Ca = \eta R^3 \dot\gamma/\kappa$, where κ is the bending modulus of the particle membrane and $\dot\gamma$ is a typical shear rate of the imposed flow. In the absence of particles, a steady-state Poiseuille flow, with a profile $u = u_m[1 - 4(r/W)^2]$ in feeding channels, is designated, where u_m is the maximum velocity, r is the lateral position in the channel, and W is the channel's width. The fluid incompressibility also imposes a $u/2$ velocity in branches. We define $\dot\gamma = 2u_m/W$ as the mean shear rate in the feeding channel. Each vessel segment has a length $40R$ ($\sim$100 μm) and a width $4R$ ($\sim$10 μm) in this study (the effect of different widths is also considered in [23]), which is consistent with microcirculation context [15,21,24]. We examine the effect of multistage bifurcations on the motion of particles with different membrane stiffnesses (different Ca's).

Dynamics of a single particle.—First, we consider a single particle in the whole network and analyze its trajectory. This provides an interesting basis for the understanding of the many particle behavior. In order to highlight the effect of particle shape adaptation, we first consider the behavior of a fully rigid circular particle (undeformable). The particle follows the fluid streamlines and shows a zigzaglike trajectory without global lateral migration within the network [Fig. 1(b), black particle]. Our simulation for a high reduced area (close to a circular shape and weak deformation) agrees with this prediction, showing again a zigzaglike trajectory [$\nu = 0.96$ in Fig. 1(c)].

In view of the above results one might naively be tempted to expect that a noncircular but rigid particle will have behavior closer to the circular particle. Surprisingly, a rigid enough particle but far from a circular shape (i.e., $\nu = 0.7$) does not follow the trend of a circular particle, while in contrast a softer particle displays a closer behavior to the circular one [Fig. 1(c)]. The results show that a softer particle exhibits an erratic trajectory [$\nu = 0.7$, Ca = 25 in Fig. 1(c)], whereas a rigid particle reveals a deterministic sideways drift [$\nu = 0.7$, Ca = 2.5 in Fig. 1(c)]. The same behavior is also observed in 3D [23].

The understanding of this behavior is quite subtle. For a small reduced area, a rigid particle assumes a constant tank-treading inclination angle [$\nu = 0.88$, 0.8, 0.7 and Ca = 2.5 in Fig. 1(c)]. If the particle is initially close to its right wall [top of Fig. 1(b), magenta particle], when it approaches the bifurcation, its orientation points towards its left branch, conferring it a higher probability to enter that branch. Once it enters the branch, the particle stays again close to its right wall of the new branch, and finds itself in the same configuration as in the previous feeding channel, and so on, giving rise to a sideways drift [see, e.g., $\nu = 0.7$, Ca = 2.5 in Fig. 1(c)]. We refer to this case as a long memory behavior. This behavior is associated with a significant particle shape deviation from a circle, and a strong rigidity.

The situation is different for a soft particle. The particle is deformed into a parachute shape instead of the slipper
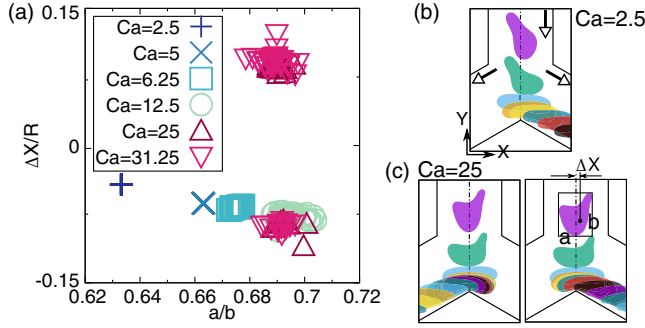
FIG. 2. (a) Deviation of the particle mass center from channel centerline (ΔX) versus deformation a/b measured at the midpoint of the feeding channel for different Ca. The bifurcation of ΔX shows that the single particle starts to erratically enter the branch when Ca is approximately larger than 12.5. (b),(c) The time series of particle configurations at a bifurcation are given for (b) Ca $= 2.5$ and (c) Ca $= 25$.

FIG. 3. (a) and (b) The time evolution of particle positions under the condition of (a) Ca $= 20$ and (b) Ca $= 2$. (c) and (d) The concentration profile along the lateral direction (X) at different times, corresponding to the configurations shown in (a) and (b).

shape in the rigid situation. Because of its quasisymmetrical shape when the particle hits the bifurcation, it has approximately equal probabilities to select either branch at the bifurcation [Fig. 1(b), blue particle]. A systematic analysis reveals that when Ca increases, we observe a distribution of deformations a/b [the size ratio defined in Fig. 2(c)] and lateral positions ΔX [Fig. 2(c)] at the midpoint of the successive feeding channels [Fig. 2(a)]. The variability broadens upon increasing Ca and the sideways preference of entering a definite branch (left or right) is lost when Ca is approximately larger than 12.5 [Fig. 2(a)]. We refer to this case as a short memory behavior.

In summary, for a shape significantly far away from a circle, a soft enough particle undergoes a random walk at bifurcation and adopts a diffusionlike spreading [the mean squared displacement (MSD) behaves as $\sim t$] along the lateral direction in the network. A more rigid particle shows a deterministic drift and exhibits a ballistic behavior, with a MSD behaving as $\sim t^2$. The observations for a single particle, lead us to expect similar phenomena for the many-particle systems, at low concentrations (where particle-particle interactions are not dominant).

Lateral transport.—Next, we focus on how an initially centered suspension spreads out laterally (in X direction) throughout the network. First, we consider the propagation of a suspension front in a network with lateral size of about $2000R$ (corresponding to 28 unit network hexagonal cells). The particles are initially positioned randomly in the middle of the network (within a range of $160R$) with a high local concentration (around 40%, with $N = 600$ particles). A typical passage time $t_0 = (L/u_m) + (L/0.5u_m) = (3L/u_m)$ is defined as the convection time through a feeding channel and a branch (L is the length of the branch [Fig. 1(a)]). We then use a normalized time as $t^* = t/t_0$. The particles are advected by the flow, while at the bifurcation, they interact with the boundaries and among each other, ultimately entering a branch (left or right).
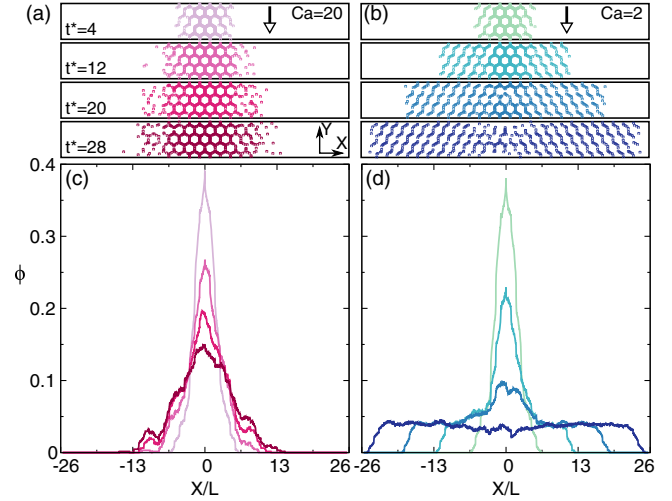
For a large Ca (corresponding to soft particles), the front of the particle distribution spreads out laterally (along X) with a diffusionlike behavior [Figs. 3(a) and 3(c) for Ca $= 20$]. In contrast, when Ca is small (corresponding to rigid particles), a systematic drift of the particle front is observed [Figs. 3(b) and 3(d) for Ca $= 2$]. We refer to the last regime as a drift regime.

The dynamics of particles is quantified by measuring the MSD in the lateral direction (MSD $= \langle |X(t) - X_0|^2 \rangle$), where $X(t)$ is the actual particle lateral position. The measurements are carried out for two values of Ca $= 20$ and Ca $= 2$ corresponding to soft and rigid particles in Figs. 3(a) and 3(b), respectively. For each capillary number, we examine five cases with different values of the imposed velocities. More precisely, we keep Ca fixed while selecting five different imposed speeds and five different bending moduli. Different parametric curves are presented with different symbols in Fig. 4(a). The selected velocities yield particle Reynolds numbers from 0.1 to 1. The data collapse obtained in Fig. 4(a) demonstrates that the observed behaviors are dominated by the particle deformability, and suggests a minor impact of the inertia effects. For Ca $= 20$ (soft particles) the MSD shows a $t^{1.4}$ scaling [Fig. 4(a)], while for Ca $= 2$ (rigid particles), it behaves as $t^{2.7}$ [Fig. 4(a)]. We have explored a wide range of Ca's, from 1 to 20, identifying a continuous evolution of the scaling exponent α, from a high value 2.7 (for Ca < 4) to a low value 1.4 (for Ca > 10) [Fig. 4(b)]. The observed many particle dynamics shows agreement with the prediction based on the individual particle dynamics. The exponents 1.4 and 2.7 of the MSD to superdiffusive and superballistic values are obtained, instead of diffusive (exponent equal to 1) and ballistic (exponent equal to 2) regimes. These large
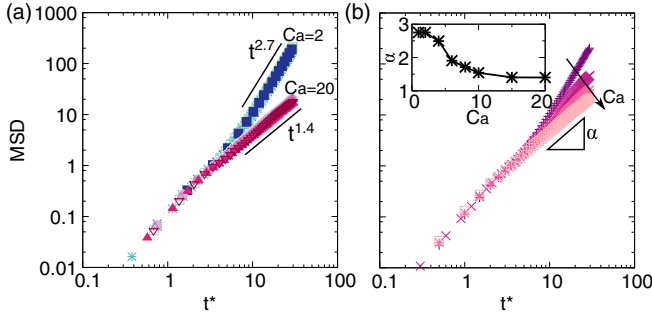
FIG. 4. (a) Lateral mean squared displacement (in X direction) of the particles for two capillary numbers (Ca = 2 and Ca = 20) with five implementations (shown by different symbols). (b) Lateral MSD for various Ca. The inset shows the scaling exponent α as a function of Ca.

values of the exponents are understood as follows: The local concentration in the central feeding vessels becomes weaker with time. Since the driving pressure is fixed, the flow rate increases with time in the feeding vessels due to the local concentration decline (see quantification of this effect in Fig. S2 in [23]). This time-dependent speed naturally amplifies the front speed, explaining the apparent tendency of a superdiffusive and superballistic nature, shown in Fig. 4. We show below that by enforcing a homogeneous concentration in the network true diffusive and ballistic behaviors are recovered [dilute regime in Fig. 5(c)].

Particle-particle collision-induced diffusion.—Here, instead of initializing a suspension in the central part of the network, we consider an initially homogeneous distribution in the whole network. This configuration can be encountered, for example, in microcirculation; the RBCs are expected (on average) to uniformly explore the network, instead of having a free front spreading laterally throughout the network. We consider a smaller size $146.6R \times 127R$ (2 unit network hexagonal cells in the lateral direction) with periodic boundary conditions. We analyze the trajectory of each particle and measure the
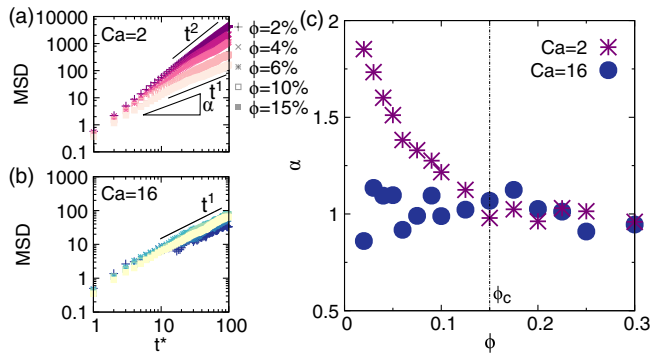

FIG. 5. (a) and (b) Lateral MSD for various ϕ with (a) Ca = 2 and (b) Ca = 16. (c) The scaling exponent of MSD as a function of ϕ.

MSD, which is averaged over all particles [Fig. 5]. We identify various regimes, going continuously from drift to anomalous diffusion and then to classical diffusion, when particle mechanical properties and concentrations are varied. In a marked contrast with anomalous diffusion in complex disordered media (e.g., porous media [29]), our geometry is ordered.

The particles are evenly and randomly initialized in the whole network. When concentration increases, the particle-particle interaction becomes relevant, leading to random partition at bifurcations [34]. This suppresses the deterministic drifting for rigid particles. Note that the diffusion-like transport for the soft particle is unaffected [$Ca = 16$ in Figs. 5(b) and 5(c)]. For rigid particles [$Ca = 2$ in Figs. 5(a) and 5(c)], in the dilute regime, as expected, we find a ballistic regime. However, the scaling exponent of the lateral MSD decreases when the concentration increases [Figs. 5(a) and 5(c)] and the lateral transport shows a diffusive behavior, similar to that exhibited by the soft particles. This drift-diffusion transition occurs for a critical volume fraction $\phi_c \simeq 15\%$ [Fig. 5(c)]. Interestingly, this concentration lies in the range of typical hematocrits in human microcirculation (10%–26% [35]). Particle-particle interaction may thus help in partially achieving an efficient random exploration of vascular networks by RBCs, even when RBCs suffer enhanced rigidity due to blood diseases, such as sickle cell and malaria diseases.

Conclusions.—We have studied the influence of deformability on the lateral transport of deformable particles in a honeycomb network. We find that the individual dynamics of the particle in the downstream position is history dependent. This results in a rich behavior when the particle meets a bifurcation. Overall, the softer particles explore different shapes from one bifurcation to the next, resulting in an erratic displacement in the network. At the dilute regime, the more rigid particles are found to drift indefinitely (when particle-particle interaction is negligible) sideways (ballistic behavior) either to the left part or the right part of the network, depending on initial conditions. For a higher concentration, the combination of particle mechanical properties and their mutual interactions leads to anomalous diffusion.

Recent experiments on a single monocyte passing a network reported that the more rigid cells follow a periodic zigzag motion without global lateral displacement [36]. This opposite behavior may be attributed to the strong confinement in the monocyte experiment. Our simulations for smaller channel widths agree with experimental observations [36] (see Fig. S3 in [23]). We have considered here an ideal honeycomb network to reduce the complexity and focus only on mechanical properties. Real vascular networks are quite disordered [37], for which our LBM can straightforwardly be adapted in the future. Besides helping understand blood flow under physiological and pathological conditions in microcirculation, this study may also shed

light on biomedical applications such as the design of appropriate networks for cell sorting and the conception of tailored microparticles for a targeted drug delivery.

---

[*]chaouqi.misbah@univ-grenoble-alpes.fr

[1] S. Marbach, K. Alim, N. Andrew, A. Pringle, and M. P. Brenner, Pruning to Increase Taylor Dispersion in Physarum Polycephalum Networks, Phys. Rev. Lett. **117,** 178103 (2016).

[2] F. J. Meigel and K. Alim, Flow rate of transport network controls uniform metabolite supply to tissue, J. R. Soc. Interface **15,** 20180075 (2018).

[3] A. Erlich, P. Pearce, R. P. Mayo, O. E. Jensen, and I. L. Chernyavsky, Physical and geometric determinants of transport in fetoplacental microvascular networks, Sci. Adv. **5,** eaav6326 (2019).

[4] F. J. Meigel, P. Cha, M. P. Brenner, and K. Alim, Robust Increase in Supply by Vessel Dilation in Globally Coupled Microvasculature, Phys. Rev. Lett. **123,** 228103 (2019).

[5] A. R. Pries, T. W. Secomb, P. Gaehtgens, and J. Gross, Blood flow in microvascular networks. Experiments and simulation, Circ. Res. **67,** 826 (1990).

[6] P. Kennel, J. Dichamp, C. Barreau, C. Guissard, L. Teyssedre, J. Rouquette, J. Colombelli, A. Lorsignol, L. Casteilla, and F. Plouraboué, From whole-organ imaging to in-silico blood flow modeling: A new multi-scale network analysis for revisiting tissue functional anatomy, PLoS Comput. Biol. **16,** e1007322 (2020).

[7] L. R. Huang, E. C. Cox, R. H. Austin, and J. C. Sturm, Continuous particle separation through deterministic lateral displacement, Science **304,** 987 (2004).

[8] R. Lu, Z. Wang, A.-V. Salsac, D. Barthès-Biesel, W. Wang, and Y. Sui, Path selection of a train of spherical capsules in a branched microchannel, J. Fluid Mech. **923,** A11 (2021).

[9] Z. Wang, Y. Sui, A.-V. Salsac, D. Barthès-Biesel, and W. Wang, Path selection of a spherical capsule in a microfluidic branched channel: Towards the design of an enrichment device, J. Fluid Mech. **849,** 136 (2018).

[10] N. Champagne, R. Vasseur, A. Montourcy, and D. Bartolo, Traffic Jams and Intermittent Flows in Microfluidic Networks, Phys. Rev. Lett. **105,** 044502 (2010).

[11] O. Cybulski, P. Garstecki, and B. A. Grzybowski, Oscillating droplet trains in microfluidic networks and their suppression in blood flow, Nat. Phys. **15,** 706 (2019).

[12] S. Choi, T. Ku, S. Song, C. Choi, and J.-K. Park, Hydrophoretic high-throughput selection of platelets in physiological shear-stress range, Lab Chip **11,** 413 (2011).

[13] Q. Guo, S. P. Duffy, K. Matthews, E. Islamzada, and H. Ma, Deformability based cell sorting using microfluidic ratchets

enabling phenotypic separation of leukocytes directly from whole blood, Sci. Rep. **7,** 6627 (2017).

[14] P. Sajeesh and A. K. Sen, Particle separation and sorting in microfluidic devices: a review, Microfluid. Nanofluid. **17,** 1 (2014).

[15] T. W. Secomb, Blood flow in the microcirculation, Annu. Rev. Fluid Mech. **49,** 443 (2017).

[16] A. Rahimian, S. K. Veerapaneni, and G. Biros, Dynamic simulation of locally inextensible vesicles suspended in an arbitrary two-dimensional domain, a boundary integral method, J. Comput. Phys. **229,** 6466 (2010).

[17] B. Quaife and G. Biros, High-volume fraction simulations of two-dimensional vesicle suspensions, J. Comput. Phys. **274,** 245 (2014).

[18] P. Balogh and P. Bagchi, Analysis of red blood cell partitioning at bifurcations in simulated microvascular networks, Phys. Fluids **30,** 051902 (2018).

[19] Z. Shen, G. Coupier, B. Kaoui, B. Polack, J. Harting, C. Misbah, and T. Podgorski, Inversion of hematocrit partition at microfluidic bifurcations, Microvasc. Res. **105,** 40 (2016).

[20] Q. Zhou, J. Fidalgo, M. O. Bernabeu, M. S. Oliveira, and T. Krüger, Emergent cell-free layer asymmetry and biased haematocrit partition in a biomimetic vascular network of successive bifurcations, Soft Matter **17,** 3619 (2021).

[21] A. Mantegazza, F. Clavica, and D. Obrist, In vitro investigations of red blood cell phase separation in a complex microchannel network, Biomicrofluidics **14,** 014101 (2020).

[22] Y. Chen, D. Li, Y. Li, J. Wan, J. Li, and H. Chen, Margination of stiffened red blood cells regulated by vessel geometry, Sci. Rep. **7,** 15253 (2017).

[23] See Supplemental Material at http://link.aps.org/supplemental/10.1103/PhysRevLett.130.014001 for a detailed description of supplemental figures.

[24] A. S. Popel and P. C. Johnson, Microcirculation and hemorheology, Annu. Rev. Fluid Mech. **37,** 43 (2005).

[25] L. Risser, F. Plouraboue, P. Cloetens, and C. Fonta, A 3d-investigation shows that angiogenesis in primate cerebral cortex mainly occurs at capillary level, International Journal of developmental neuroscience : the official Journal of the International Society for Developmental Neuroscience **27,** 185 (2009).

[26] A. R. Pries and T. W. Secomb, Blood flow in microvascular networks, in Microcirculation (Elsevier, New York, 2008), pp. 3–36, 10.1016/B978-0-12-374530-9.00001-2.

[27] C. Pozrikidis, Numerical simulation of blood flow through microvascular capillary networks, Bull. Math. Biol. **71,** 1520 (2009).

[28] D. Obrist, B. Weber, A. Buck, and P. Jenny, Red blood cell distribution in simplified capillary networks, Phil. Trans. R. Soc. A **368,** 2897 (2010).

[29] X.-R. Yang and Y. Wang, Ubiquity of anomalous transport in porous media: Numerical evidence, continuous time random walk modelling, and hydrodynamic interpretation, Sci. Rep. **9,** 4601 (2019).

[30] K. Araki, Y. Furuya, M. Kobayashi, K. Matsuura, T. Ogata, and H. Isozaki, Comparison of mucosal microvasculature between the proximal and distal human colon, Microscopy **45,** 202 (1996).

[31] Z. Shen, A. Farutin, M. Thiébaud, and C. Misbah, Interaction and rheology of vesicle suspensions in confined shear flow, Phys. Rev. Fluids **2**, 103101 (2017).

[32] T. Krüger, F. Varnik, and D. Raabe, Efficient and accurate simulations of deformable particles immersed in a fluid using a combined immersed boundary lattice boltzmann finite element method, Comput. Math. Appl. **61**, 3485 (2011).

[33] T. Krüger, S. Frijters, F. Günther, B. Kaoui, and J. Harting, Numerical simulations of complex fluid-fluid interface dynamics, Eur. Phys. J. Special Topics **222**, 177 (2013).

[34] X. Wang, M. Hossain, A. Bogoslowski, P. Kubes, and D. Irimia, Chemotaxing neutrophils enter alternate branches at capillary bifurcations, Nat. Commun. **11**, 2385 (2020).

[35] Y.-C. Fung, *Biomechanics: Circulation* (Springer Science & Business Media, New York, 2013), 10.1007/978-1-4757-2696-1.

[36] J. Dupire, P.-H. Puech, E. Helfer, and A. Viallat, Mechanical adaptation of monocytes in model lung capillary networks, Proc. Natl. Acad. Sci. U.S.A. **117**, 14798 (2020).

[37] P. Balogh and P. Bagchi, Direct numerical simulation of cellular-scale blood flow in 3d microvascular networks, Biophys. J. **113**, 2815 (2017).